Received: 10 January 2022 | Revised: 6 June 2022 | Accepted: 19 July 2022

DOI: 10.1002/cnm.3638

BASIC RESEARCH

WILEY

Toward modeling thrombosis and thromboembolism in laminar and turbulent flow regimes

Nicolas Tobin[1] | **Keefe B. Manning**[1,2]

[1]Department of Biomedical Engineering, The Pennsylvania State University, University Park, Pennsylvania, USA

[2]Department of Surgery, Penn State Hershey Medical Center, Hershey, Pennsylvania, USA

Correspondence
Keefe B. Manning, 122 Chemical and Biomedical Engineering Building, The Pennsylvania State University, University Park, PA 16802-4400, USA.
Email: kbm10@psu.edu

Funding information
National Institutes of Health, Grant/Award Number: R01HL136369; National Science Foundation, Grant/Award Numbers: 2017805, ACI-1548562; National Heart, Lung, and Blood Institute

Abstract

Thrombosis and thromboembolism are deadly risk factors in blood-contacting biomedical devices, and in-silico models of thrombosis are attractive tools to understand the mechanics of these processes, though the simulation of thromboembolism remains underdeveloped. The purpose of this study is to modify an existing computational thrombosis model to allow for thromboembolism and to investigate the behavior of the modified model at a range of flow rates. The new and existing models are observed to lead to similar predictions of thrombosis in a canonical backward-facing step geometry across flow rates, and neither model predicts thrombosis in a turbulent flow. Simulations are performed by increasing flow rates in the case of a clot formed at lower flow to induce embolization. While embolization is observed, most of the clot breakdown is by shear rather than by breakup and subsequent transport of clotted material, and further work is required in the formulation and validation of embolization. This model provides a framework to further investigate thromboembolization.

KEYWORDS

thromboembolism, thrombosis, turbulent, viscoelastic

1 | INTRODUCTION

Thrombosis and thromboembolism (T&TE) are centrally important life-threatening complications in patients with implanted blood-contacting medical devices such as blood pumps, artificial valves, and stents. Daeman et al.[1] observed an incidence of thrombosis at a rate of .01 events per patient year (EPPY) in patients with coronary stents. For prosthetic heart valves, obstructive thrombosis occurs at between .003 and .013 EPPY, while thromboembolic complications occur between .007 and .06 EPPY.[2] T&TE occur at particularly high rates in modern blood pumps; Strueber et al.[3] reported an incidence of stroke at a rate of .08 EPPY, pump thrombosis at a rate of .09 EPPY, and thrombosis-related pump replacement at a rate of .03 EPPY in a post-market analysis of patients receiving a HeartWare ventricular assist device (HVAD) in the European Union and Australia. Other observations of stroke incidence in heart pumps are as high as .18 EPPY.[4]

T&TE in blood-contacting devices involves intricately connected interactions between the biochemistry of the coagulation cascade, contact of blood with foreign materials, flow patterns and stagnation, and platelet activation. As opposed to the tissue-factor-initiated extrinsic coagulation cascade due to endothelial injury, the coagulation cascade in implanted devices is understood to be initiated by the surface activation of Factor XII,[5] and activation of platelets by abnormal shear-stress distributions and by other procoagulant factors. In device thrombosis, the accumulation of

procoagulant factors produces a stable thrombus primarily composed of activated platelets, cross-linked fibrin, and entrapped red blood cells. The subsequent interaction between the fluid dynamics and the mechanics of the blood clot, as well as biochemical effects of plasmin or thrombolytic drugs,[6] has the potential to cause the clot to dislodge, resulting in thromboembolism. This can lead to complications as serious as pulmonary embolism or stroke.

The need to better understand the processes of T&TE in blood-contacting devices makes in-silico models attractive, as a much richer understanding of the localized environment is possible including stresses exerted on a blood clot, local concentrations of procoagulant species, and high-resolution flow field data, though challenges remain including a disconnect between physiological and numerical timescales, experimental validation and incorporating pathologies among others.[7] Modern in-silico T&TE models are increasingly computationally affordable, and are being used in device-specific simulations to inform thrombus risk,[8] to investigate thrombolysis in strokes,[9] and to predict venous thrombosis.[10] Fogelson and Guy[11] proposed a single-scale model based on conservation equations for resting and activated platelets, a generic activator chemical taking the place of the coagulation cascade, and viscoelastic constitutive equations for a cohesive-link tensor and a cohesive-link density. Taylor et al.[12] adapted this model with a material-specific thrombus susceptibility potential term, replacing the viscoelastic model with a Brinkman model to couple the thrombus and the flow, and trained their model on experimental data of clot growth in a backward-facing step geometry. Yang et al.[13] explored modifications to the Taylor et al.[12] model to make corrections to the biochemical activation and investigate the impact of non-Newtonian constitutive models on thrombus growth.

However, these models are still far from capturing all the phenomena relevant to T&TE in high-flow devices such as blood pumps. By replacing the viscoelastic model of Fogelson and Guy[11] with a Brinkman model,[14] Taylor et al.[12] precluded their model from being able to capture macroembolization as their aggregation intensity evolution equation lacked a convective term. This model was also only applied to a single laminar flow condition, which is not representative of the turbulent flows typical in heart pumps. The purpose of the current study is to modify the previously developed model of Taylor et al.[12] so that macroembolization is possible, and investigate the impacts of flow rate, including turbulent flow, on thrombus predictions to evaluate conditions where embolization could occur. This is done by returning to the original viscoelastic formulation of Fogelson and Guy,[11] while retaining important modifications from Taylor et al.[12] and Yang et al.[13] to the biochemistry and thrombus growth mechanisms. The ability of the fitted viscoelastic model to capture macroembolization is then assessed by numerically forming a clot and subsequently increasing flow rates. In the following sections, the methodologies used to numerically investigate the addition of a viscoelastic model are detailed, results are presented of thrombosis and embolization simulations across Reynolds number and modeling approach, and the significance of these results is discussed.

2 | MATERIALS & METHODS

2.1 | Taylor model and modifications from Yang et al

The current model shares most aspects with that of the Taylor[12] model, for which an overview is given here. The Taylor[12] model solves the Navier–Stokes momentum equation with a Brinkman term as in Equations (1) and (2). Equation (1), as well as all subsequent equations, uses the Einstein notation of summation over repeated indices. In Equation (1), u_i is the i-th component of velocity, p is the pressure, ν is the kinematic viscosity, and $F(\varepsilon)$ is the Brinkman function. In Equation (2), k is the clot permeability, ε is the aggregation intensity, and ε_t is a threshold aggregation intensity.

$$\frac{\partial u_i}{\partial t}+u_j\frac{\partial u_i}{\partial x_j}=-\frac{1}{\rho}\frac{\partial p}{\partial x_i}+\frac{\partial}{\partial x_j}\left(\nu\left[\frac{\partial u_i}{\partial x_j}+\frac{\partial u_j}{\partial x_i}\right]\right)-\nu F(\varepsilon)u_i, \tag{1}$$

$$F(\varepsilon)=\begin{cases}0, \varepsilon<\varepsilon_t\\ \frac{1}{k}\frac{\varepsilon/\varepsilon_t}{\varepsilon/\varepsilon_t+1}, \varepsilon\geq\varepsilon_t\end{cases}. \tag{2}$$

In parallel with the solution of the momentum equation, a set of convection-diffusion–reaction equations is solved for activated and unactivated platelets, given in Equations (3) and (4). In these equations, ϕ_n is the concentration of

unactivated platelets, ϕ_a is the concentration of activated platelets, D_p is platelet diffusivity, A_c is the rate of biochemical activation, and A_m is the rate of mechanical platelet activation.

$$\frac{\partial \phi_n}{\partial t} + u_k \frac{\partial \phi_n}{\partial x_k} = D_p \frac{\partial^2 \phi_n}{\partial x_j \partial x_j} - [A_c + A_m]\phi_n, \tag{3}$$

$$\frac{\partial \phi_a}{\partial t} + u_k \frac{\partial \phi_a}{\partial x_k} = D_p \frac{\partial^2 \phi_a}{\partial x_j \partial x_j} + [A_c + A_m]\phi_n. \tag{4}$$

The mechanical activation A_m is based on the power-law model of Soares et al.,[15] and takes the form:

$$A_m = \left(1 - \phi_f\right) C^{\frac{1}{\beta}} \beta \phi_f^{\frac{\beta-1}{\beta}} \tau^{\frac{\alpha}{\beta}}, \tag{5}$$

where $\phi_f = \phi_a/(\phi_a + \phi_n)$ is the fraction of total platelets which are activated, τ is a scalar shear stress as defined in Taylor et al.,[12] and C, α, and β are fitted constants. Chemical activation happens in response to adenosine diphosphate (ADP) concentration and takes the form given in Equation (6), where t_{ADP} is a time scale of chemical platelet activation, and ADP_t is a threshold ADP concentration for platelet activation.

$$A_c(\text{ADP}) = \begin{cases} 0, \text{ADP} < \text{ADP}_t \\ \dfrac{\text{ADP}}{\text{ADP}_t \times t_{\text{ADP}}}, \text{ADP} \geq \text{ADP}_t \end{cases}. \tag{6}$$

ADP follows a convection-diffusion–reaction equation, and is released when platelets are activated, as in Equation (7), where D_{ADP} is the diffusivity of ADP, and R_{ADP} is the amount of ADP released per activated platelet.

$$\frac{\partial \text{ADP}}{\partial t} + u_k \frac{\partial \text{ADP}}{\partial x_k} = D_{\text{ADP}} \frac{\partial^2 ADP}{\partial x_j \partial x_j} + R_{\text{ADP}}[A_c + A_m]\phi_n. \tag{7}$$

Finally, an evolution equation is solved for the aggregation intensity as given in Equation (8). This aggregation intensity is used to determine the magnitude of the Brinkman term in Equation (2), which is subsequently used in Equation (1) to reduce velocity in regions of high aggregation intensity. Equation (8) includes a growth constant α_ε and a decay function β_ε.

$$\frac{d\varepsilon}{dt} = \alpha_\varepsilon P_{\text{TSP}}(\tau_w)\phi_a^2 - \beta_\varepsilon(\tau_w)\varepsilon. \tag{8}$$

The form of P_{TSP}, the thrombus susceptibility potential, is given in Equation (9) as a function of the wall shear stress τ_w. The thrombus susceptibility potential is depicted in Figure 1, and is intended to allow clots to form in regions of low wall shear stress, while disallowing clotting in regions of high wall shear stress. In Equation (9), τ_w is the wall shear stress, and τ_{high} and τ_{low} are upper and lower threshold wall shear stresses for thrombus growth.

$$P_{\text{tsp}}(\tau_w) = \begin{cases} 1, |\tau_w| \leq \tau_{\text{low}} \\ 1 - \dfrac{|\tau_w|}{\tau_{\text{high}}} \times \dfrac{\exp\left(\dfrac{|\tau_w| - \tau_{\text{low}}}{\tau_{\text{high}} - \tau_{\text{low}}}\right) - 1}{e^1 - 1}, \quad \tau_{\text{low}} < |\tau_w| < \tau_{\text{high}} \\ 0, |\tau_w| \geq \tau_{\text{high}} \end{cases}. \tag{9}$$

Finally, breakdown of the aggregation intensity is modeled with the term β_ε given in Equation (10), where $\tau_{\text{breakdown}}$ is a threshold wall shear stress.

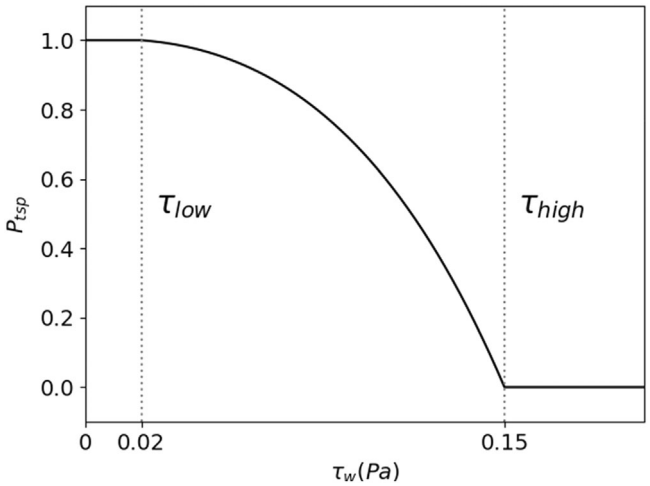

FIGURE 1 Thrombus susceptibility potential function as described in Equation (7). The dependence of thrombus susceptibility potential on wall shear stress allows clots to form in regions of low wall shear stress, and not in regions of high wall shear stress

TABLE 1 Simulation details of varying flow rates investigated

Flow rate	Reynolds number	Simulation type	Simulation time (min)
.20 LPM	100	Laminar	15
.39 LPM	200	Laminar	15
.76 LPM (matching Yang et al.[13])	388	Laminar	15
1.18 LPM	600	Laminar	15
1.96 LPM	1000	Laminar	15
3.93 LPM	2000	Laminar	10
6.87 LPM	3500	Implicit LES	2.8

$$\beta_e(\tau_w) = \begin{cases} 0, \tau_w < \tau_{\text{breakdown}} \\ \beta, \tau_w \geq \tau_{\text{breakdown}} \end{cases}. \tag{10}$$

The parameter values used in the various equations of the Taylor model are given in Table 1 of Taylor et al.[12] Taylor et al.[12] also performed blood-loop experiments to train and validate the derived model. Yang et al.[13] later made modifications to the Taylor[12] model, in particular incorporating a different model for chemical platelet activation, since the Taylor[12] model never reached high enough levels of ADP to lead to chemical platelet activation. The Yang et al.[13] chemical activation model is used in the current iteration of the thrombosis model, and is given in Equation (11). Yang et al.[13] also investigated the use on non-Newtonian viscosity models, which are not incorporated into the current study.

$$A_c = k_{\text{ADP}} \frac{\text{ADP}^4}{\text{ADP}_t^4 + \text{ADP}^4}. \tag{11}$$

2.2 | Implementation of the cohesive stress model

The cohesive-stress model of Fogelson and Guy[11] is implemented into a custom OpenFOAM[16] solver to replace the use of the Brinkman term in the model of Taylor et al.[12] This requires a modification to the aggregation intensity equation to include a convective term as in Equation (12), as well as using a different form of the breakage function, detailed

later. In Equation (12), ϵ is the viscoelastic aggregation intensity, α_1 is an undetermined growth constant, B is a breakage function, and σ_{ii} is the trace of the cohesive stress tensor.

$$\frac{\partial \epsilon}{\partial t} + u_i \frac{\partial \epsilon}{\partial x_i} = P_{\text{tsp}} \alpha_1 \phi_a^2 - B\left(\frac{\sigma_{ii}}{\epsilon}\right)\epsilon. \tag{12}$$

In addition, an evolution equation (Equation (13)) is solved for the cohesive stress tensor, which couples the thrombus to the velocity field and represents the mechanical effect of a clot. The left-hand side of Equation (13) denotes an upper-convected time derivative, ensuring frame-invariance of the tensor evolution equation; α_2 is another undetermined growth constant, and δ_{ij} is the Kronecker delta.

$$\frac{\partial \sigma_{ij}}{\partial t} + u_k \frac{\partial \sigma_{ij}}{\partial x_k} - \frac{\partial u_i}{\partial x_k}\sigma_{kj} - \frac{\partial u_j}{\partial x_k}\sigma_{ik} = P_{\text{tsp}} \alpha_2 \phi_a^2 \delta_{ij} - B\left(\frac{\sigma_{kk}}{\epsilon}\right)\sigma_{ij}. \tag{13}$$

Taken together, Equations (12) and (13) constitute the "approximate closure" model of Fogelson and Guy.[11] However, missing from Fogelson and Guy are prescribed values for α_1 and α_2 and a functional form for $B\left(\frac{\sigma_{kk}}{\epsilon}\right)$, the breakage function present in both equations. The parameters α_1 and α_2 are integrals of a cohesive link formation-rate function $\alpha(\|\boldsymbol{y}\|)$ over the microscale spatial variable $\boldsymbol{y}$. We prescribe a formation-rate function as in Equation (14), where L_f is the mean length of a fibrin strand and $\widetilde{A}$ is an undetermined rate constant. We then perform the integrals described in Fogelson and Guy,[11] and derive definitions of α_1 and α_2 in Equations (15) and (16), where $S = EA_f/L_f$ is the stiffness of a fibrin strand, E is the Young's modulus of a fibrin strand and A_f is its cross-sectional area. The form of Equation (14) is prescribed with the assumption that links are most likely to form when the separation between two points is small compared to the length of a fibrin strand, and the link formation should go to zero at distances much larger than this length.

$$\alpha(\|\boldsymbol{y}\|) = \widetilde{A} \exp\left(-\frac{\|\boldsymbol{y}\|^2}{2L_f^2}\right), \tag{14}$$

$$\alpha_1 = \int_{\boldsymbol{y}} \alpha(\|\boldsymbol{y}\|) d\boldsymbol{y} = \frac{\widetilde{A}}{8}\pi^{3/2} L_f^3, \tag{15}$$

$$\alpha_2 = \int_{\boldsymbol{y}} \frac{1}{2}\alpha(\|\boldsymbol{y}\|) S \|\boldsymbol{y}\|^2 d\boldsymbol{y} = \frac{3\widetilde{A}}{32}\pi^{3/2} S L_f^5. \tag{16}$$

Because $\widetilde{A}$ is an unknown constant, we define $A = \widetilde{A}\pi^{3/2}/8$ so that $\alpha_1 = AL_f^3$ and $\alpha_2 = \frac{3}{4}AEA_f L_f^4$. The link formation source term is therefore defined up to the constants A, E, A_f, and L_f. Fogelson and Guy[11] also show that the argument of the breakage function B is proportional to the mean squared microscale fiber length. Consistent with their derivation, we take the form in Equation (17) as the argument of the breakage function as it is a measure of squared strain.

$$e^2 = 2\frac{\sigma_{kk}}{SL_f^2\epsilon}. \tag{17}$$

We adopt a specific form for B similar to equation (112) from Guy,[17] who investigated the performance of various breakage functions. This form is given in Equation (18), where e_t is the threshold fiber strain above which breakage increases from its background rate B_0. As fibrin fibers can elastically stretch to approximately three times their length before permanent damage,[18] e_t is set as 3. This form has the property that $B(0) = B_0 > 0$, so that Equations (6) and (8) do not grow unbounded while breakage still increases with increased strain. Due to the forms of α_1 and α_2, newly formed cohesive links will have a strain of $(9/2)^{1/2} \approx 2.12$ and therefore do not have above-background breakage.

$$B(e^2) = \begin{cases} B_0, e^2 < e_t^2 \\ B_0 \dfrac{e^2}{e_t^2}, e^2 \geq e_t^2 \end{cases}. \tag{18}$$

Equations (6) and (8) are solved at every time step, and the impact of the thrombus on the flow is implemented by including the divergence of the cohesive stress tensor into the momentum equation (Equation (19)).

$$\frac{\partial u_i}{\partial t} + u_j \frac{\partial u_i}{\partial x_j} = -\frac{1}{\rho}\frac{\partial p}{\partial x_i} + \frac{\partial}{\partial x_j}\left(\nu\left[\frac{\partial u_i}{\partial x_j} + \frac{\partial u_j}{\partial x_i}\right]\right) + \frac{1}{\rho}\frac{\partial \sigma_{ij}}{\partial x_j}. \tag{19}$$

2.3 | Backward-facing step simulations

Simulations are performed in the same backward-facing step geometry as both Taylor et al.[12] and Yang et al.[13] This geometry consists of a tube with a diameter of 1 cm, and a 2.5 mm step, creating a recirculating region where clots are observed to form in the MRI data. The grid used in the simulations extended 6 cm upstream and downstream of the step, had a maximum streamwise grid spacing of 600 μm, a maximum spanwise and vertical spacing of 300 μm, doubled grid resolution in the recirculation region, and sufficient near-wall resolution to ensure that $y^+ < 1$ at all Reynolds numbers. The grid is depicted in Figure 2, along with a higher-resolution grid that is subsequently used for grid convergence analysis. The low-resolution grid contained approximately 800,000 finite-volume elements.

Backward Euler time differencing was used, and spatial differencing for the convective term of all field variables except for the cohesive stress tensor used a blend of 75% second-order linear and 25% second-order upwind differencing. The convective term of the cohesive stress tensor used a van Albada[19] limiter. All other gradient terms used second-order linear differencing. All residuals were converged at each time step to 10^{-8}.

Simulations were run with the goal of matching the human-blood experimental conditions of Yang et al.[20] Unlike in Yang et al.,[13] blood was assumed Newtonian with a kinematic viscosity of 4.4 cSt, and the total concentration of platelets (activated and unactivated) was set to 185,000/μl matching the platelet concentration reported in the human samples of Yang et al.,[20] with an initial platelet activation of 5%, which was used as the initial condition in Taylor et al.[12] To replicate the closed-loop MRI experiments of Yang et al.[20] and produce a fully developed inlet velocity boundary condition, inlet boundary conditions of ADP, activated and unactivated platelets and velocity used a recycled boundary condition, mapping downstream values as inlet boundary conditions. These inlet values were interpolated based on the values 1 cm upstream of the step, replicating recirculation of factors in the closed loop. This approach resulted in well-mixed ADP and platelet concentrations approaching the step, with an asymptotic ADP concentration of 5.3 μM and asymptotic platelet activation of 100% reached in approximately 3.5 min. This varied from the work of both Taylor et al.[12] and Yang et al.,[13] who effectively simulated fresh blood continually entering the domain. Both the aggregation intensity and the cohesive stress tensor were set to zero at the inlet, enforcing no influx of clotted blood.

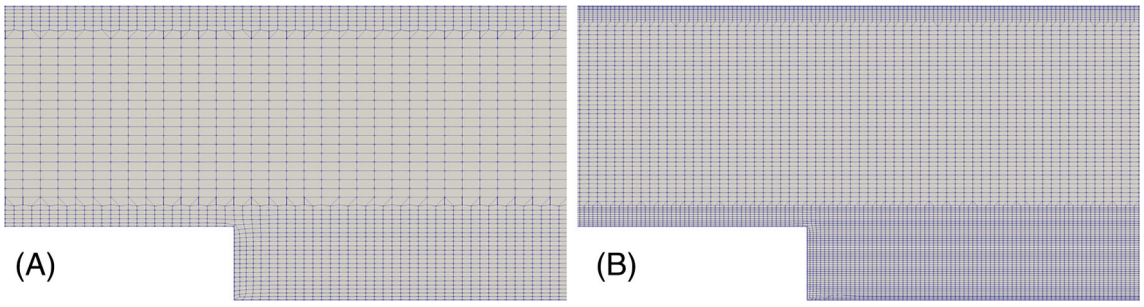

FIGURE 2 Portion of the computational grid near the backward-facing step; (A) low-resolution grid with largest streamwise spacing of 600 μm, largest spanwise and vertical spacing of 300 μm, and 800,000 finite-volume elements; (B) high-resolution grid with largest streamwise spacing of 300 μm, largest spanwise and vertical spacing of 150 μm, and 5.2 million finite-volume elements

To assess the impact of flow rate, including turbulent flow, varying flow rates were investigated ranging from .20 LPM to 6.87 LPM. A list of specific cases is provided in Table 1. At the highest flow rate, with a Reynolds number of 3500, simulations were solved using an implicit large-eddy simulation (LES) approach, resolving large-scale turbulent motions. To compare differences between the Brinkman and viscoelastic models, all simulations were repeated using the unaltered model and boundary conditions of Yang et al.[13] with a Newtonian viscosity assumption. Simulations using the Brinkman model were run for 30 min. However, because the solution of the viscoelastic equations requires a much smaller time step (particularly at high flow rates), viscoelastic simulations were run until both the platelet activation and thrombus volume reached a steady state or 15 min, whichever came first. On 64 processors, the viscoelastic simulations took between approximately 1 day and 1 week. The Brinkman simulations took at most 10 h. All viscoelastic simulations as well as the turbulent Brinkman simulation used dynamic time-stepping to maintain a maximum Courant number of less than .5. This maintained a time-step of approximately 1×10^{-3} s for the lowest flow rate (Re = 100) and approximately 2×10^{-5} s for the highest flow rate (Re = 3500).

While traditional LES would include a model for the subgrid-scale (SGS) stress, implicit LES does not, and simply relies on numerical dissipation to act as an energy sink, effectively modeling the SGS stress as zero. Therefore, the same momentum equation (Equation (14)) is solved during both laminar and turbulent simulations. This decision was made to avoid modeling interactions between the SGS stress and the cohesive stress. A detailed overview of implicit LES can be found in Grinstein, Margolin, and Rider.[21] No comparison was made in the current study to other SGS models in the BFS. Instead, the accuracy of the implicit LES simulations was determined based on grid convergence only.

2.4 | Grid and time-step sensitivity study

A grid sensitivity analysis was performed by doubling the grid resolution in every direction, resulting in a high-resolution grid with approximately 5.2 million grid elements. Comparisons were made between grid resolutions of (1) profiles of velocity in the .76 LPM case, (2) profiles of time-averaged velocity in the 6.87 LPM case, (3) clot shape over time in the .76 LPM case, and (4) maximum aggregation intensity in the 6.87 LPM case. Due to the high computational cost of the fine-grid turbulent simulation, the initial condition assumed that platelets were 100% activated, thrombosis simulations were run for 5 s to achieve steady maximum aggregation intensity, and the steady-state maximum aggregation intensity is compared between the two grid resolutions.

Brinkman simulations were run with time-steps consistent with those used in Taylor et al.[12] and Yang et al.,[13] with a maximum Courant number of 5. All simulations were also run with a maximum Courant number of 10 to establish time-step independence.

2.5 | Embolization simulations

The primary goal for the proposed alterations to the Taylor[12] model is to be able to simulate macroembolization. To evaluate the ability of the viscoelastic model to capture macroembolization, the final timepoint of the MRI-matching case was used as an initial condition for four additional simulations, where the flow rate was increased to match the higher-flow conditions (i.e., Reynolds numbers of 600, 1000, 2000, and 3500). These simulations were run for 1 second with snapshots saved every .01 s to better quantify fast embolization dynamics.

2.6 | Selection of parameters

The present model requires the selection of several parameters. Many of the parameter values used in the current study are identical to those used in Taylor et al.[12] and Yang et al.,[13] though additional values are required relating to the viscoelastic model. All parameter values are laid out in Table 2 along with the justification for those values. While most parameters are based on literature values, specific values of A and B_0 are found by fitting to the experimental MRI data of Yang et al.[20] In addition, whether a cell is designated as "thrombus" is determined by whether the aggregation intensity is above a threshold ϵ_t. This is also determined based on the current results.

TABLE 2 Thrombosis model parameter values and sources

Parameter	Value	Source
D_p	1.58×10^{-7} cm^2/s	22
D_{ADP}	2.37×10^{-6} cm^2/s	23
C	1.4854×10^{-7}	15
α	1.4854	15
β	1.4401	15
R_{ADP}	3×10^{-17} moles/platelet	24
k_{ADP}	.05 s^{-1}	13
τ_{low}	.02 Pa	12
τ_{high}	.15 Pa	12
L_f	9.2 μm	25
E	1.7 MPa	25
D_f	284 nm	25
e_t	3	18
ADP_t	2 μM	26
A	2.2×10^{-6} s^{-1}	Fitted to data from Yang et al.[16]
B_0	1.5×10^{-4} s^{-1}	Fitted to data from Yang et al.[16]
ϵ_t	1×10^4/ml	Based on reduction in shear rate

2.7 | Turbulent thrombosis experiments

In order to validate computational thrombosis predictions at the highest Reynolds number, experiments were run with an identical protocol to that of Taylor et al.[12] at a flow rate of approximately 6.9 LPM. In short, 450 ml of bovine blood were collected into a bag containing 63 ml of CDPA-1 anticoagulant and kept at room temperatures until the experiment was performed. Immediately before the experiment, blood was recalcified with calcium chloride solution to achieve a calcium ion concentration of 11 mM to reverse the effect of the anticoagulant.

Flow was driven through an acrylic model of the backward-facing step with a peristaltic pump (Cole-Parmer 77602-10, Vernon Hills, IL). After 15 min, the loop was slowly drained with phosphate-buffered saline, and the model was visually inspected for the presence of clots. The flow loop experiment was repeated twice ($n = 2$).

3 | RESULTS

3.1 | Thrombus constants

Because a threshold on ϵ is used to designate a given finite volume element as a thrombus, an appropriate value for this threshold must be determined. Because the hallmark of a thrombus is the ability to arrest flow, the reduction in local shear rate across all grid elements in shown in Figure 3A as a function of the local aggregation intensity. An aggregation intensity of 10^4/ml is found to reduce the local shear rate by approximately 75%; this value is therefore used as the aggregation intensity threshold.

Exact values of A and B_0 were found by trial and error to reproduce the volume growth curve from the MRI data. Values of $A = 2.2 \times 10^{-6}$ and $B_0 = 1.5 \times 10^{-4}$ were found to fit the MRI data well and are used in subsequent simulations. A sensitivity analysis to these parameters is shown in Figure 3B and Figure 3C. In Figure 3B, simulations denoted as "A" had $B_0 = 1 \times 10^{-4}$, "B" denoted $B_0 = 1.5 \times 10^{-4}$ and "C" denoted $B_0 = 2 \times 10^{-4}$; similarly, simulations denoted "1" had $A = 1.5 \times 10^{-6}$, while "2" and "3" correspond to $A = 2.2 \times 10^{-6}$ and $A = 3 \times 10^{-6}$, respectively. The specific cases and parameter values are detailed in Table 3. Depicted in Figure 3C are the root-mean-square Z-scores (Equation (15)) of the simulated clot volume with varying values of A and B_0. In Equation (20), V_c^i is the i-th computational volume, V_e^i is the i-th experimental volume, and σ_V^i is the i-th experimental standard deviation of volume, where $i = 1, 2$, and

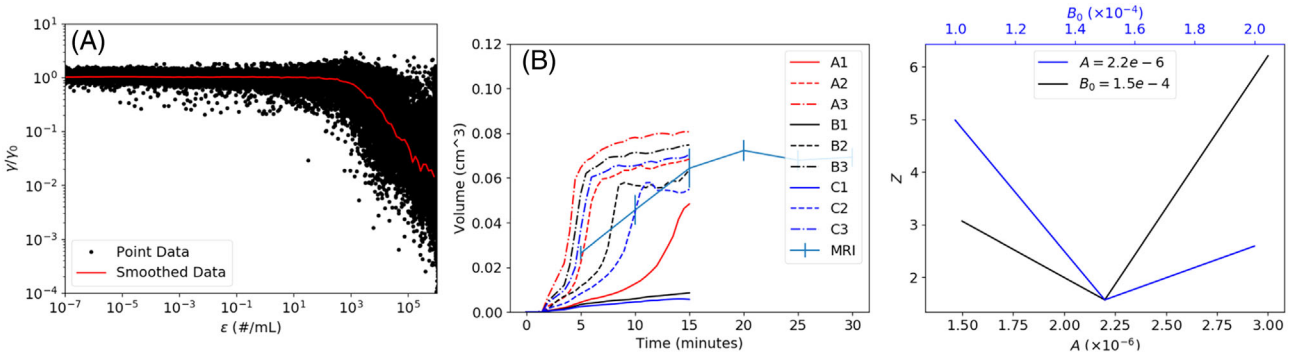

FIGURE 3 Determination and sensitivity of clot parameters; (A) reduction in shear rate as a function of aggregation intensity shows an inflection in reduction at around 10^4/ml; (B) clot volume growth with varying constitutive parameters shows a wide range in predictions despite a small range in parameter values; (C) 15-min clot volume shows a strong sensitivity of clot volume to the growth parameter A, and a more modest sensitivity to the decay constant B_0.

TABLE 3 Parameter values used in parameter sensitivity study

	A	***B***	***C***
1	$A = 1.5 \times 10^{-6}$	$A = 1.5 \times 10^{-6}$	$A = 1.5 \times 10^{-6}$
	$B_0 = 1 \times 10^{-4}$	$B_0 = 1.5 \times 10^{-4}$	$B_0 = 2 \times 10^{-4}$
2	$A = 2.2 \times 10^{-6}$	$A = 2.2 \times 10^{-6}$	$A = 2.2 \times 10^{-6}$
	$B_0 = 1 \times 10^{-4}$	$B_0 = 1.5 \times 10^{-4}$	$B_0 = 2 \times 10^{-4}$
3	$A = 3 \times 10^{-6}$	$A = 3 \times 10^{-6}$	$A = 3 \times 10^{-6}$
	$B_0 = 1 \times 10^{-4}$	$B_0 = 1.5 \times 10^{-4}$	$B_0 = 2 \times 10^{-4}$

3 correspond to data at 5, 10, and 15 min. Based on the results depicted in Figure 3C, the values of $A = 2.2 \times 10^{-6}$ and $B_0 = 1.5 \times 10^{-4}$ are at or near a local minimum on agreement with experimental clot volume.

$$Z = \left[\frac{1}{3}\sum_{i=1}^{3}\left(\frac{V_c^i - V_e^i}{\sigma_V^i}\right)^2\right]^{1/2}. \tag{20}$$

3.2 | Grid and time-step sensitivity

Figure 4A depicts a comparison between velocity profiles in the low-resolution and high-resolution simulations for the MRI-matching flow rate (Re = 388). Figure 4B similarly depicts the time-averaged velocity profiles for the highest flow-rate, turbulent case (Re = 3500). The root-mean-square error comparing high-resolution and low-resolution solutions in the MRI-matching case was 1.1% of the mean velocity at the inlet; for the turbulent case, this was 2.3%. The velocity is therefore considered well-converged with the lower grid resolution across Reynolds number. Figure 4C depicts the volume growth curves of the low-resolution and high-resolution clots at the MRI-matching case of .76 LPM. At 15 min, the high-resolution clot is approximately 12% larger in volume, .7% greater in length, and 1.6% greater in height than the low-resolution clot. The time-averaged steady-state maximum aggregation intensity in the 6.87 LPM case was approximately 6% higher in the high-resolution case than in the low-resolution case. The lower-resolution grid is therefore accepted for its performance in the convergence of clot evolution, and all subsequent simulations are performed on the lower-resolution grid.

3.3 | Validation with MRI data of BFS thrombus growth

Using the fitted parameters $A = 2.2 \times 10^{-6}$, $B_0 = 1.5 \times 10^{-4}$, the clot volume over time shows similar agreement with the MRI data as the Brinkman model does, as shown in Figure 5. At 15 min, the two models and the MRI data have clot

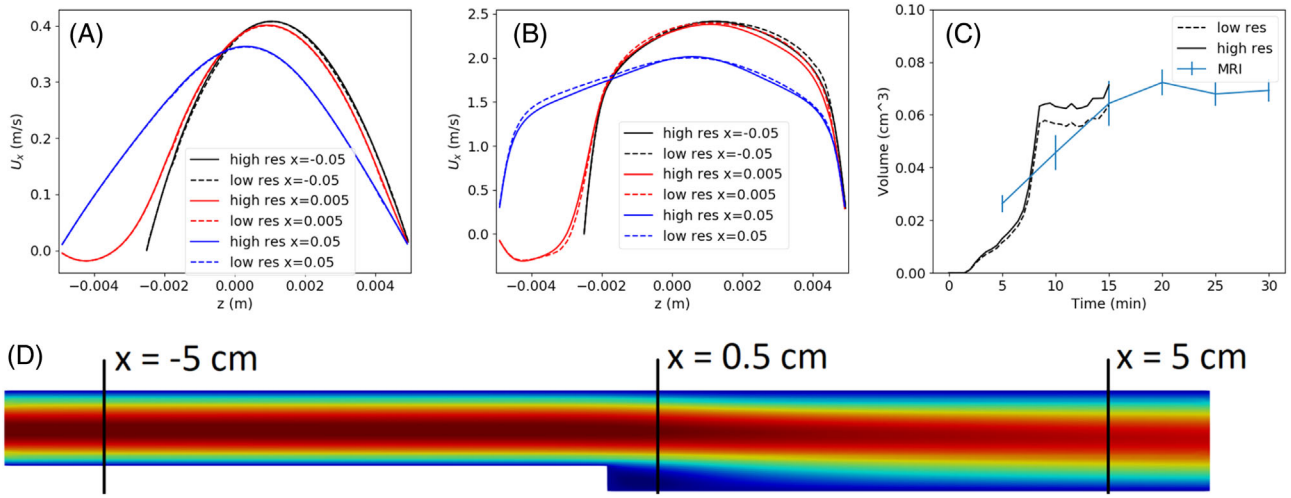

FIGURE 4 Comparison of low-resolution and high-resolution solutions for (A) velocity at Re = 388; (B) time-averaged velocity at Re = 3500; (C) clot growth with two grid resolutions over 15 min; (D) locations of velocity profiles overlaid on Re = 388 case. Profiles in black are taken 5 cm before the step. Profiles in red are taken .5 cm after the step, within the recirculation zone for both Reynolds numbers. Profiles in blue are taken 5 cm after the step. Solid lines indicate high-resolution solutions, while dashed lines indicates low-resolution solutions

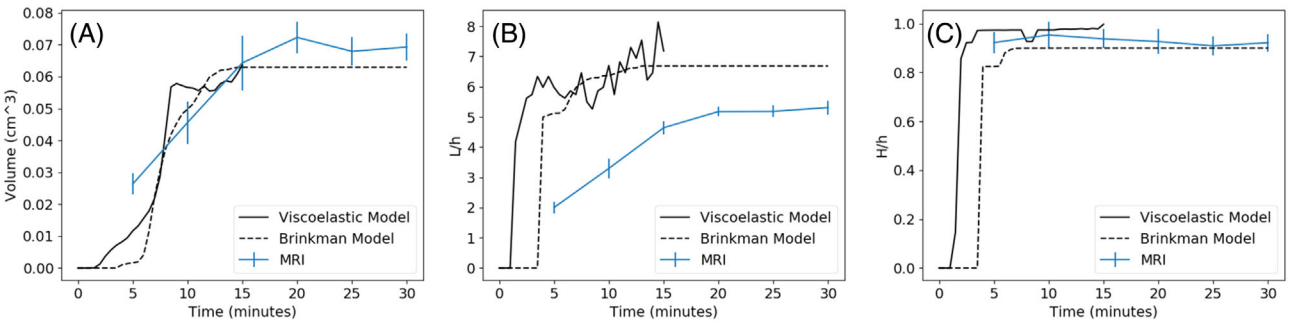

FIGURE 5 Comparison between MRI experimental data, viscoelastic model, and Brinkman model. (A) clot volume over time; (B) clot length over time; (C) clot height over time. Laminar flow at MRI-matching conditions (Re = 388)

volumes within 3% of each other; however, there is modest disagreement between the two models and the experimental data at 5 min and 10 min. The height of the clot also agrees very well with both the data and the Brinkman model. However, both the Brinkman model and the viscoelastic model overpredict clot length. At early times, this is due to the formation of a clot at the end of the recirculation zone, which was not observed in experiments. Both models predict early thrombosis both at the base of the step and at the end of the recirculation zone, with the two clots eventually merging. While this merged clot is more consistent with the experimental data, the length remains overpredicted even at later time points.

3.4 | Flow rate effects

3.4.1 | Laminar flow

Both the viscoelastic and Brinkman models led to complex growth behavior as a function of Reynolds number in the laminar regime, as shown in Figure 6. In general, clot volume decreased as a function of Reynolds number. However, clot length decreased with Reynolds number until reaching a minimum at the MRI-matching case (Re = 388) and subsequently increasing again. At lower flow rates, longer clots formed despite shorter recirculation lengths due to lower levels of wall shear. However, at higher flow rates, both models predict clots forming in two distinct regions without

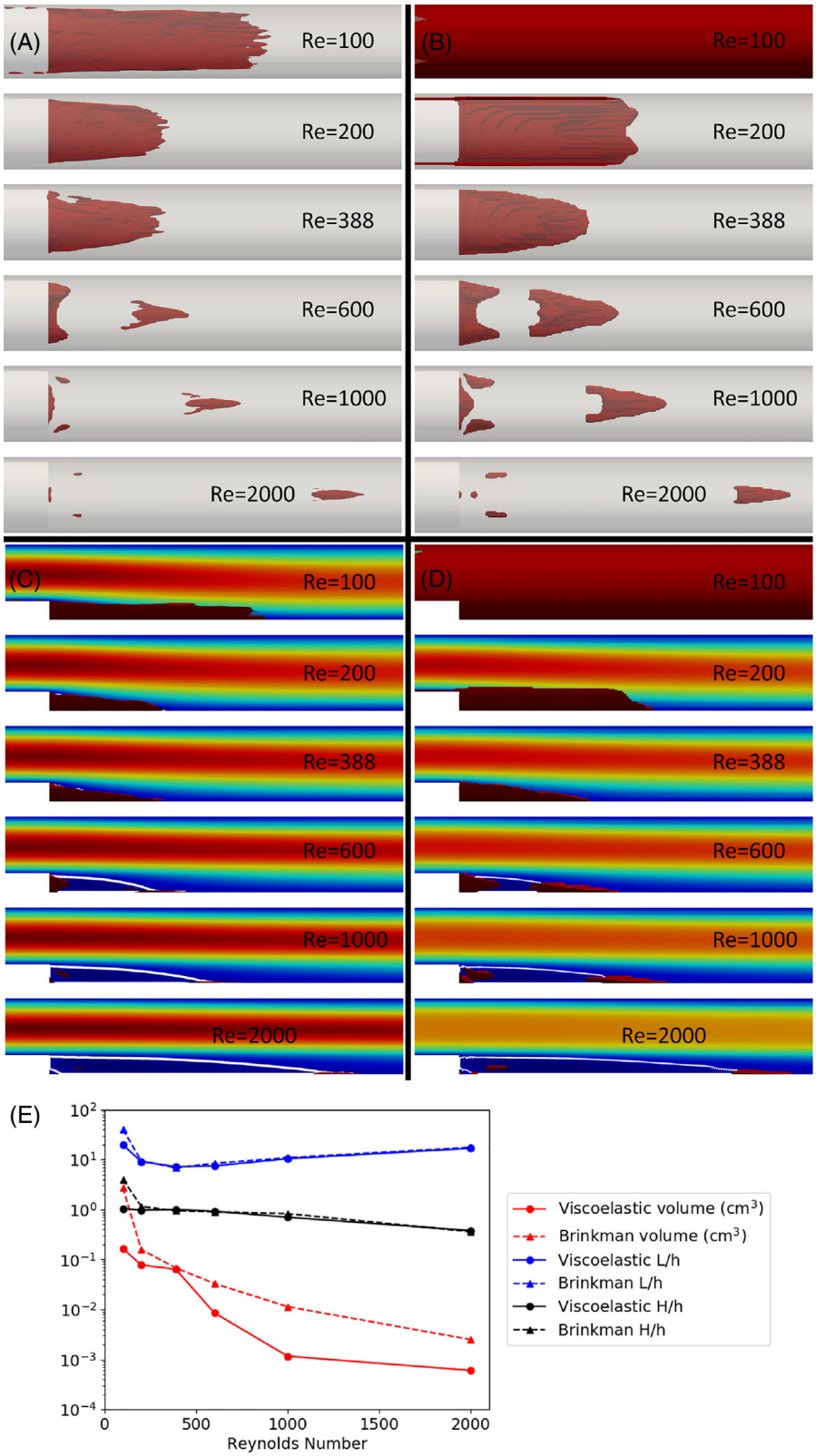

FIGURE 6 Depictions of final-time clots (15 min or converged clot) across Reynolds numbers. (A) top view of viscoelastic model; (B) top view of Brinkman model; (C) side view of viscoelastic model with streamwise velocity contour normalized by mean velocity at the inlet, and white line indicating zero streamwise velocity; (D) side view of Brinkman model with streamwise velocity contour normalized by mean velocity at the inlet, and white line indicating zero streamwise velocity; (E) volume, length, and height plotted as a function of Reynolds number

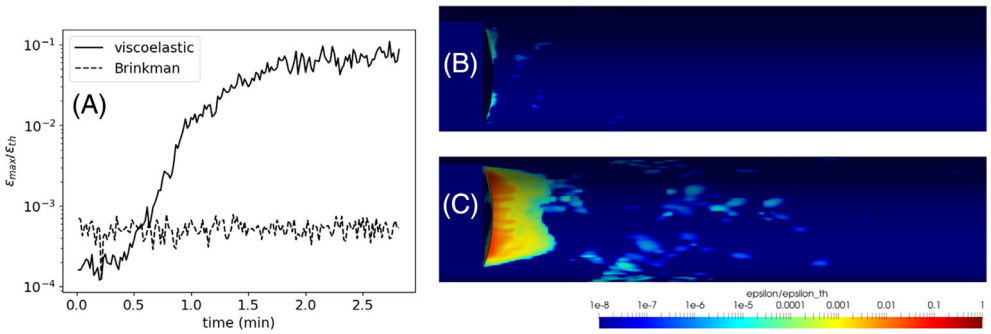

FIGURE 7 Behavior of aggregation intensity at Re = 3500. (A) Time course of maximum aggregation intensity; normalized aggregation intensity contours on the bottom wall of the BFS model with (B) the Brinkman model and; (C) the viscoelastic model

converging. Specifically, clotted material is observed near the base of the step and at a downstream region corresponding to the end of the recirculation zone, where wall shear is locally low. The border of the recirculation zone is depicted in Figure 6 with a white contour where the streamwise velocity is equal to zero. At higher Reynolds numbers, the length of the recirculation zone increases, resulting in a clot length that grows with Reynolds number above the MRI-matching case.

3.4.2 | Turbulent flow

At the highest flow rate, corresponding to Re = 3500, no clot is formed with either model. As shown in Figure 7, the maximum values of ϵ over the domain for both models fail to reach their respective threshold values. While the maximum aggregation intensity increases over approximately 2.5 min with the viscoelastic model, the maximum values fluctuate around a mean with the Brinkman model due to the difference in inlet boundary condition for activated platelets.

3.5 | In-vitro turbulent-flow clotting experiments

No formed clot was visible in the turbulent flow experiments.

3.6 | Embolization simulations

Figure 8 depicts the macroembolization process in the Re = 2000 case. For each time point, the thrombus is colored by the local fiber strain, which is the determinant of local link breakage. At early time points, fiber strain is low. Between 0 and .14 s, a mass of thrombus is advected downstream, and the center of this mass remains at relatively low strain. This mass undergoes necking behavior near the clot's anchor point, where a thin section of clot undergoes high fiber strain, on the order of 50, before the clot embolizes. This high strain corresponds to a local breakage rate of $\sim\frac{50^2}{3^2}$, or 278 times the background breakage rate. Strain is also locally high at the upper surface of the clot, where the fluid shear layer imposes high velocity gradients. The apparent lengthening and subsequent shortening of the clot in Figure 8 is primarily due to out-of-plane movement of the embolizing structure.

Shown in Figure 9 are the volume over time, and the total cohesive links over time in the embolization simulations at varying Reynolds number. Counterintuitively, the thrombus volume increases at first at all Reynolds numbers, and subsequently decreases at all Reynolds numbers except for Re = 600. However, it should be noted that the equations as cast do not conserve thrombus volume but do conserve link density; as seen in Figure 9B, the total number of cohesive links decreases sharply at the highest Reynolds number, with a less pronounced decrease at lower Reynolds numbers, even resulting in a slight increase at Re = 600. Despite the decay in total number of cohesive links, macroembolization was minor. Instead, link breakage accounted for greater than 98% of the reduction in total link number at Reynolds number of 1000 and above; the remaining small fraction of link number reduction was due to links exiting the domain through the outlet. Despite the minimal impact of macroembolization, simulations were

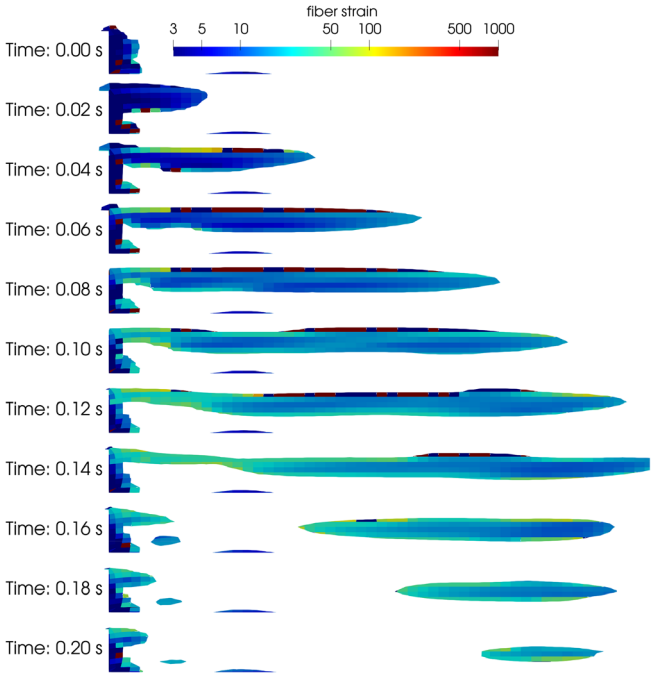

FIGURE 8 Cross-sectional view of the embolization process in the Re = 2000 case. Contours depict local fiber strain, showing an accumulation of high strain in the neck, which subsequently breaks, causing embolization

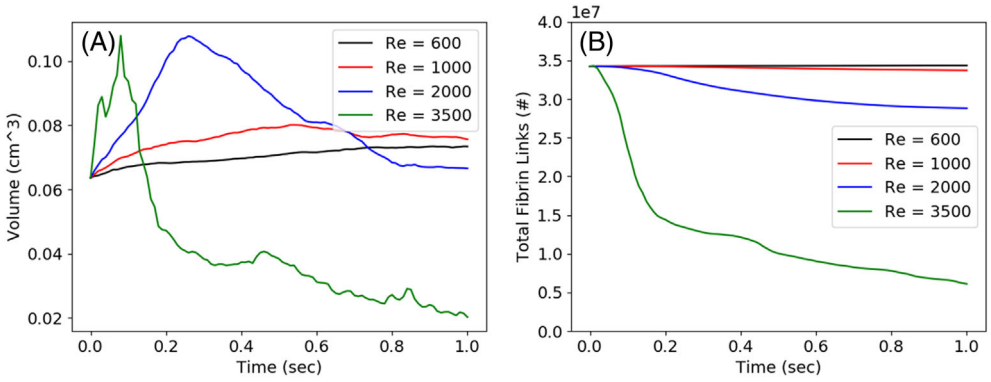

FIGURE 9 (A) clot volume over time and; (B) total fibrin links over time after start of embolization simulations

able to produce instances of thromboemboli due to macroembolization breaking off the main thrombus, as shown in Supplementary Material 1.

4 | DISCUSSION

At Reynolds numbers of 200 and above, predictions from the Brinkman and viscoelastic models are broadly consistent, though the behavior at Re = 100 is divergent. The large clot that is formed by the Brinkman model at the lowest flow rate is consistent with an overall trend where the viscoelastic model leads to smaller clots. There are at least two possible reasons for this trend. First, because the results of the viscoelastic model are sensitive to the parameters A and B_0, better agreement might be found with further tweaks to these values. Second, the convective transport of aggregated material also plays a role in causing smaller viscoelastic clots, as the clot can both be broken apart and washed away in the viscoelastic case, whereas the Brinkman model has no way to advect clotted material. Despite the disagreement in clot characteristics at low flow rates, both models show similar agreement with the MRI data at .76 LPM. In the absence

of low-flow data, it is unclear which model is more representative of thrombosis at flow rates other than the MRI-matching case.

In contrast to the Brinkman model, the viscoelastic model produces data that are much noisier in time, as seen especially in the growth curves over time in Figure 5. The noisiest of the three reported statistics is the clot length. This highlights that transport is important to model in addition to growth, not only for embolization, but also for thrombus growth. The final viscoelastic clots depicted in Figure 6 show varying levels of asymmetry, while the Brinkman model produced perfectly symmetric clots. This disordered growth with the viscoelastic model is likely more realistic and could provide important information on clot heterogeneity. This information could play an important role in embolization as fault lines may correlate with heterogeneities. A recent computational experiment by Du et al.[27] similarly suggests that disordered transport of clotted material plays an important role in determining the mechanical structure of a clot under flow.

The two models as well as the in-vitro experiments agree that no clot is formed in the turbulent flow case. Although low shear rates are occasionally present near the step and slightly downstream of it, these low-shear areas are transient. Deposited thrombus is therefore quickly washed away soon after depositing, and the aggregation intensity does not reach adequate levels to be considered a thrombus. The Brinkman model is therefore not activated, and the cohesive stress term remains small in comparison to the viscous stress. Although the two models agree that no clot forms at this flow rate, some mechanism could be missing from both, such as the activity of von Willebrand factor, a protein that unfurls at high shear rates and strongly binds to foreign surfaces and platelets, resulting in clots at surfaces with high shear.[28] A continuum model of von Willebrand factor unfurling has been introduced by Zhussupbekov et al.,[29] and inclusion of such a model could be illuminating in this case.

For future efforts to validate the macroembolization of thrombi, the current results suggest that the backward-facing step will produce embolization at a range of Reynolds numbers. This may make it possible to observe and validate stratified behavior such as simple stress accumulation in a laminar embolization case, or damage accumulation from chaotic turbulent motions resulting in ultimate embolization. According to the current embolization simulations, macroembolization occurs primarily due to the clot breaking apart rather than breaking away from the wall. This will be an important consideration for future validation, as the propensity to fail within the thrombus versus failing at the wall will surely be dependent not only on the properties of the wall, but the properties of the clot, including age and histological properties such as fibrin content. For example, embolization events observed in Goodman et al.[30] corresponded to complete delaminating of adhered thrombus to the wall of a polyethylene tube suggesting embolization via failure of thrombus adhesion. In contrast, embolic events observed in the computational model of Fogelson and Guy[11] on tissue-factor mediated thrombus suggested failure in the volume of the clot. Though experimental data will not be able to provide validation of all aspects of embolization such as intra-clot fibrin strain, high-speed videography will provide insights on the kinetics of detachment and embolization.

A potential future application of the current work could be to produce an embolization risk map based simply on the fluid dynamics and clot mechanics. While there are numerous coupled biochemical and mechanical properties inherent to thrombosis and thromboembolism, embolization is ultimately a matter of the force balance and distribution on and throughout the clot.[31,32] Basic forces exerted on the clot include adhesion to the wall, cohesion within the clot, pressure gradient across the clot, and viscous drag. A theoretical investigation of these characteristics, accompanied by simulations in varying geometries, could be used to create a physics-informed risk map like that proposed by Basmidjian.[33] This could provide a useful library of embolization data to inform design decisions for blood-contacting devices.

The tendency of the current model to lead to thrombus erosion rather than macroembolization is notable. The inclusion of a post-formation stiffening might create clots that could withstand higher shear rates without breaking down; such behavior has a physiological parallel in Factor XIII, which cross-links fibrin bonds and strengthens clots.[34] Such a modeling approach may tip the balance from erosion to macroembolization, and more accurately predict embolization risk. However, the production of sub-threshold levels of aggregation intensity and the erosion rather than macroembolization of thrombus could inform risk factors related to microembolization. Spontaneous erosion of thrombus can lead to microinfarction and coronary infarction,[35] as well as increasing pulmonary vascular resistance,[36] potentially allowing the current model to inform both risk factors.

5 | LIMITATIONS

At the MRI-matching condition, a clot is predicted at the downstream edge of the recirculation zone, while no such clot was observed in the experiments of Yang et al.[20] or Taylor et al.[12] This discrepancy was also noted in Taylor et al.[12] and

Yang et al.,[13] but the reason for the discrepancy remains elusive. Unsteady flow due to the roller pumps both in the experiments of Taylor et al.[12] and Yang et al.[20] likely caused the reattachment point to migrate during the cycle of the pump. This would appear to be consistent with the observations of the current turbulent flow case, where transient low wall shear rates result in some deposited clot, but that deposited clot is quickly washed away due to shifting flow patterns. This discrepancy may be responsible for the overprediction of both models of the clot's length.

The goal of the current work is to evaluate the ability of the viscoelastic model to produce instances of macroembolization. However, it seems likely based on the current results that macroembolization is not realistically reproduced. Although the ability of small parts of the formed thrombus to break away and be carried by the flow is made clear by the visualizations in the Supplementary Material, the behavior of these emboli is not realistic. Despite large reductions in total cohesive links at the highest Reynolds number indicate clot breakdown, most of this reduction is due to breakdown rather than parts of the clot breaking off and exiting the domain, which is in contrast to some in-vitro embolization data.[30] There are several reasons why this discrepancy could be happening. The simulated clot may simply not be stiff enough. That is, the magnitude of the cohesive stress tensor must be larger. At the end of the 15-min MRI-matching simulation, the clot had a modulus of around 50 Pa, much lower than typical values of at least 1 kPa.[37] However, in the current formulation of the viscoelastic model, attempts to create a stiffer clot also produce larger clots, which compare poorly to the MRI. Apart from the lack of Factor XIII, another potential source of error is the functional form of the breakage function B. Although most values of fiber strain throughout the domain were found to be close to their resting length of 2.12, values occasionally go as high as 10^6 during embolization simulations, resulting in very high breakage. The breakage function may need to be evaluated in its behavior at high strains.

Apart from the exclusion of Factor XIII and von Willebrand factor, the current formulation of the model has additional shortcomings. The platelet transport equations do not have any method for platelets to marginate to the walls,[38] or for platelets to accumulate above their background concentration in the clot. Since activated platelets tend to adhere to solid surfaces, the assumption that activated platelets simply continue to circulate freely in the blood is suspect. In addition, although it is assumed that platelet–platelet links are formed by fibrin strands, the current model does not explicitly track fibrinogen, its polymerization into fibrin, or fibrin concentration. The current model would also benefit from a more sophisticated representation of the coagulation cascade,[39,40] potentially missing important transport phenomena associated with the stagnation region of the backward-facing step. This is especially relevant as the thrombus produced in Taylor et al.[12] was mostly red. Although the current formulation has parallels with coagulation-induced thrombosis, with accumulation of ADP similar to accumulation of thrombin and formation of platelet–platelet links conceptually similar to the formation of a fibrin mesh, it would be ideal to produce a formulation that was able to separately model white and red thrombi.

6 | CONCLUSION

A viscoelastic constitutive model is implemented into the thrombosis model developed by Taylor et al.[12] and Yang et al.,[13] and fitted to existing MRI data of human blood flow in a backward-facing step. The predictions of the viscoelastic model are compared to those from the older Brinkman model across Reynolds number, and the ability of the viscoelastic model to produce macroembolization is investigated. The two models produce similar thrombosis predictions across Reynolds number, and similar agreement with the MRI data. The viscoelastic model is able to produce small instances of macroembolization, but the majority of the clot is simply sheared apart rather than embolized.

Future work will go toward conceptually understanding why the current formulation of the viscoelastic model produces poor macroembolization results, and will focus on post-formation stiffening of clots, different formulations for link breakage, and matching the resulting mechanical properties to experimental viscoelastic data on clots. Future work will also prioritize validation of the embolization aspect of the model.

ACKNOWLEDGMENTS

Research reported in this publication was supported by the National Heart, Lung, and Blood Institute of the National Institutes of Health under award (R01HL136369). This material is based upon work supported by the National Science Foundation under Grant (CMMI-2017805). This work used the Extreme Science and Engineering Discovery Environment (XSEDE), which is supported by National Science Foundation grant (ACI-1548562). The authors would like to acknowledge the efforts of Michael Daly in performing the flow-loop experiments.

CONFLICT OF INTEREST

The authors declare no potential conflict of interest.

DATA AVAILABILITY STATEMENT

The data that support the findings of this study are available from the corresponding author upon reasonable request.

ORCID

Keefe B. Manning https://orcid.org/0000-0001-9029-5217

REFERENCES

1. Daemen J, Wenaweser P, Tsuchida K, et al. Early and late coronary stent thrombosis of sirolimus-eluting and paclitaxel-eluting stents in routine clinical practice: data from a large two-institutional cohort study. *Lancet*. 2007;369(9562):667-687.
2. Roudaut R, Serri K, Lafitte S. Thrombosis of prosthetic heart valves: diagnosis and therapeutic considerations. *Heart*. 2007;93(1):137-142.
3. Strueber M, Larbalestier R, Jansz P, et al. Results of the post-market registry to evaluate the HeartWare left ventricular assist system (ReVOLVE). *J Heart Lung Transplant*. 2014;33(5):486-491.
4. Miller LW, Pagani FD, Russell SD, et al. Use of a continuous-flow device in patients awaiting heart transplantation. *N Engl J Med*. 2007;357(9):885-896.
5. Zhuo R, Siedlecki CA, Vogler EA. Autoactivation of blood factor XII at hydrophilic and hydrophobic surfaces. *Biomaterials*. 2006;27(24):4325-4332.
6. Dimitrov K, Maier J, Sandner S, et al. Thrombolysis as first-line therapy for Medtronic/HeartWare HVAD left ventricular assist device thrombosis. *Eur J Cardio-Thorac Surg*. 2020;58(6):1182-1191.
7. Manning KB, Nicoud F, Shea SM. Mathematical and computational modeling of device-induced thrombosis. *Curr Opin Biomed Eng*. 2021;20:100349.
8. Méndez Rojano R, Zhussupbekov M, Antaki JF. Multi-constituent simulation of thrombus formation at LVAD inlet cannula connection: importance of Virchow's triad. *Artif Organs*. 2021;45:1014-1023.
9. Manchester EL, Roi D, Gu B, Xu XY, Lobotesis K. Modelling combined intravenous thrombolysis and mechanical thrombectomy in acute Ischaemic stroke: understanding the relationship between stent retriever configuration and clot lysis mechanisms. *Life*. 2021;11(11):1271.
10. Bouchnita A, Terekhov K, Nony P, Vassilevski Y, Volpert V. A mathematical model to quantify the effects of platelet count, shear rate, and injury size on the initiation of blood coagulation under venous flow conditions. *PLoS One*. 2020;15(7):e0235392.
11. Fogelson AL, Guy RD. Immersed-boundary-type models of intravascular platelet aggregation. *Comput Methods Appl Mech Eng*. 2008;197(25):2087-2104.
12. Taylor JO, Meyer RS, Deutsch S, Manning KB. Development of a computational model for macroscopic predictions of device-induced thrombosis. *Biomech Model Mechanobiol*. 2016;15(6):1713-1731.
13. Yang L, Tobin N, Manning KB. Refining a numerical model for device-induced thrombosis and investigating the effects of non-Newtonian blood models. *J Biomech*. 2021;120:110393.
14. Leiderman K, Fogelson AL. Grow with the flow: a spatial-temporal model of platelet deposition and blood coagulation under flow. *Math Med Biol*. 2011;28(1):47-84.
15. Soares JS, Sheriff J, Bluestein D. A novel mathematical model of activation and sensitization of platelets subjected to dynamic stress histories. *Biomech Model Mechanobiol*. 2013;12(6):1127-1141.
16. Weller HG, Tabor G, Jasak H, Fureby C. A tensorial approach to computational continuum mechanics using object-oriented techniques. *Comput Phys*. 1998;12(6):620-631.
17. Guy RD. Asymptotic analysis of PTT type closures for network models with variable junction concentrations. *J Non-Newton Fluid Mech*. 2004;123(2–3):223-235.
18. Liu W, Jawerth LM, Sparks EA, et al. Fibrin fibers have extraordinary extensibility and elasticity. *Science*. 2006;313(5787):634.
19. van Albada GD, van Leer B, Roberts WW. A comparative study of computational methods in cosmic gas dynamics. *Upwind and High-Resolution Schemes*. Springer Berlin; 1997:95-103.
20. Yang L, Neuberger T, Manning KB. In vitro real-time magnetic resonance imaging for quantification of thrombosis. *Magn Reson Mater Phys Biol Med*. 2021;34(2):285-295.
21. Grinstein FF, Margolin LG, Rider WJ. *Implicit Large Eddy Simulation*. Cambridge University Press; 2007.
22. Goldsmith HL, Turitto VT. Rheological aspects of thrombosis and haemostasis: basic principles and applications. *Thromb Haemost*. 1986;55(3):415-435.
23. Hubbell JA, McIntire LV. Platelet active concentration profiles near growing thrombi. *Biophys J*. 1986;50:937-945.
24. Holmsen H, Weiss HJ. Secretable storage pools in platelets. *Annu Rev Med*. 1979;30(1):119-134.
25. Collet J-P, Shuman H, Ledger RE, Lee S, Weisel JW. The elasticity of an individual fibrin fiber in a clot. *Proc Natl Acad Sci*. 2005;102(26):9133-9137.
26. Frojmovic MM, Mooney RF, Wong T. Dynamics of platelet glycoprotein IIb–IIIa receptor expression and fibrinogen binding. I. Quantal activation of platelet subpopulations varies with adenosine diphosphate concentration. *Biophys J*. 1994;67(5):2060-2068.

27. Du J, Aspray E, Fogelson A. Computational investigation of platelet thrombus mechanics and stability in stenotic channels. *J Biomech*. 2021;112:110398.
28. Reininger AJ, Heijnen HFG, Schumann H, Specht HM, Schramm W, Ruggeri ZM. Mechanism of platelet adhesion to von Willebrand factor and microparticle formation under high shear stress. *Blood*. 2006;107(9):3537-3545.
29. Zhussupbekov M, Méndez Rojano R, Wu W-T, Massoudi M, Antaki JF. A continuum model for the unfolding of von Willebrand factor. *Ann Biomed Eng*. 2021;49:2646-2658.
30. Goodman PD, Barlow ET, Crapo PM, Mohammad SF, Solen KA. Computational model of device-induced thrombosis and thromboembolism. *Ann Biomed Eng*. 2005;33(6):780-797.
31. Sukavaneshvar S, Zheng Y, Rosa GM, Mohammad SF, Solen KA. Thromboembolization associated with sudden increases in flow in a coronary stent ex vivo shunt model. *ASAIO J*. 2000;46(3):301-304.
32. Shi X, Yang J, Huang J, et al. Effects of different shear rates on the attachment and detachment of platelet thrombi. *Mol Med Rep*. 2016; 13(3):2447-2456.
33. Basmidjian D. Embolization: critical thrombus height, shear rates, and pulsatility. Patency of blood vessels. *J Biomed Mater Res*. 1989; 23(11):1315-1326.
34. Standeven KF, Carter AM, Grant PJ, et al. Functional analysis of fibrin γ-chain cross-linking by activated factor XIII: determination of a cross-linking pattern that maximizes clot stiffness. *Blood J Am Soc Hematol*. 2007;3:902-907.
35. Heusch G, Skyschally A, Kleinbongard P. Coronary microembolization and microvascular dysfunction. *Int J Cardiol*. 2018;258:17-23.
36. Pagnamenta A, Vanderpool R, Brimioulle S, Naeije R. Proximal pulmonary arterial obstruction decreases the time constant of the pulmonary circulation and increases right ventricular afterload. *J Appl Physiol*. 2013;114(11):1586-1592.
37. Mfoumou E, Tripette J, Blostein M, Cloutier G. Time-dependent hardening of blood clots quantitatively measured in vivo with shear-wave ultrasound imaging in a rabbit model of venous thrombosis. *Thromb Res*. 2014;133(2):265-271.
38. Hong Z, Shaqfeh ESG. Shear-induced platelet margination in a microchannel. *Phys Rev E*. 2011;83(6):061924.
39. Méndez Rojano R, Mendez S, Lucor D, et al. Kinetics of the coagulation cascade including the contact activation system: sensitivity analysis and model reduction. *Biomech Model Mechanobiol*. 2019;18(4):1139-1153.
40. Méndez Rojano R, Mendez S, Nicoud F. Introducing the pro-coagulant contact system in the numerical assessment of device-related thrombosis. *Biomech Model Mechanobiol*. 2018;17(3):815-826.

SUPPORTING INFORMATION

Additional supporting information can be found online in the Supporting Information section at the end of this article.

How to cite this article: Tobin N, Manning KB. Toward modeling thrombosis and thromboembolism in laminar and turbulent flow regimes. *Int J Numer Meth Biomed Engng*. 2022;38(10):e3638. doi:10.1002/cnm.3638